AGU PUBLICATIONS

JGR

Journal of Geophysical Research: Space Physics

RESEARCH ARTICLE

10.1002/2014JA020347

Key Points:
- The time-dependent propagation of CME from the Sun to Earth
- The analysis of the propagation velocity, shape, and trajectory of the CME
- The comparison of the simulation results with STEREO and Wind observations

Correspondence to:
X. Feng,
fengx@spaceweather.ac.cn

Citation:
Zhou, Y., X. Feng, and X. Zhao (2014), Using a 3-D MHD simulation to interpret propagation and evolution of a coronal mass ejection observed by multiple spacecraft: The 3 April 2010 event, *J. Geophys. Res. Space Physics*, *119*, 9321–9333, doi:10.1002/2014JA020347.

Received 1 JUL 2014
Accepted 5 NOV 2014
Accepted article online 11 NOV 2014
Published online 4 DEC 2014

Using a 3-D MHD simulation to interpret propagation and evolution of a coronal mass ejection observed by multiple spacecraft: The 3 April 2010 event

Yufen Zhou[1,2], Xueshang Feng[1], and Xinhua Zhao[1]

[1]SIGMA Weather Group, State Key Laboratory of Space Weather, Center for Space Science and Applied Research, Chinese Academy of Science, Beijing, China, [2]CAS Key Laboratory of Geospace Environment, Department of Geophysics and Planetary Sciences, University of Science and Technology of China, Hefei, China

Abstract The coronal mass ejection (CME) event on 3 April 2010 is the first fast CME observed by STEREO Sun Earth Connection Coronal and Heliospheric Investigation/Heliospheric Imager for the full Sun-Earth line. Such an event provides us a good opportunity to study the propagation and evolution of CME from the Sun up to 1 AU. In this paper, we study the time-dependent evolution and propagation of this event from the Sun to Earth using the 3-D SIP-CESE (Solar-InterPlanetary Conservation Element and Solution Element) MHD model. The CME is initiated by a simple spherical plasmoid model: a spheromak magnetic structure with high-speed, high-pressure, and high-plasma density plasmoid. The simulation performs a comprehensive study on the CME by comparing the simulation results with STEREO and Wind observations. It is confirmed from the comparison with observations that the MHD model successfully reproduces many features of both the fine solar coronal structure and the typical large-scale structure of the shock propagation and gives the shock arrival time at Earth with an error of ~2 h. Then we analyze in detail the several factors affecting the CME's geo-effectiveness: the CME's propagation trajectory, span angle, and velocity.

1. Introduction

Coronal mass ejections (CMEs) are spectacular events involving the expulsion of significant amounts of solar material (10^{15-16} g) into the heliosphere [*Hundhausen*, 1987], with speeds observed from 20 to 2600 km/s. Associated with this eruption is 10^{31-32} ergs of energy, which is presumably supplied by the magnetic field. They are responsible for nonrecurrent disturbances in the interplanetary medium, and their interactions with the Earth's magnetosphere cause severe geo-effective storms. It is believed that CMEs play an important role in the associated space weather effects.

It is well known that single spacecraft observation cannot directly describe the global structures of magnetic clouds and their evolution in interplanetary space due to projection effects. In situ measurements at the first Lagrangian point (L1) can give the accurate information about the plasma and magnetic field structure of CMEs but only along a one-dimensional cut through the large-scale three-dimensional structure. The determination of CME's global structure and kinematics requires in situ observations from multiple vantage points. Now we have several spacecraft looking at the Sun including the Solar and Heliospheric Observatory (SOHO; *Domingo et al.* [1995]) and the Solar Terrestrial Relations Observatory (STEREO; *Kaiser et al.* [2008]). In particular, after 2006, the NASA STEREO mission started to provide multispacecraft in situ observations [e.g., *Kilpua et al.*, 2009a; *Mostl et al.*, 2009], and image interplanetary CMEs (ICMEs) in white light along the entire Sun-Earth line [*Eyles et al.*, 2009]. STEREO is composed of two identical spacecraft orbiting the Sun ahead STEREO-A (STA) and behind STEREO-B (STB) Earth near the ecliptic plane [*Kaiser et al.*, 2008]. The two spacecraft separate away from Earth at a rate of about 22° per year. In recent years, much attention has been given to the CMEs observed by multiple spacecraft in different locations. These events are of great importance for studying their evolution process in the heliosphere. Several authors have discussed ICMEs sweeping over an in situ observing spacecraft in the Heliospheric Imager (HI) images [e.g., *Davies et al.*, 2009; *Liu et al.*, 2010, 2013; *Lee et al.*, 2013; *Prise et al.*, 2014].

However, STEREO spacecraft is at lower latitudes, and it cannot provide the high-latitude observations of CME. Thus, the real global structure of CMEs and the underlying physics governing CME propagation in the heliosphere are not well understood. The 3-D MHD solutions can provide the global structure of the event.

Hence, the 3-D numerical studies of observed CME events and comparison of the numerical results with observation data at any point are promising. Moreover, the 3-D MHD simulation results can help provide a deeper insight in space weather physics, by a careful study of the propagation characteristics. This insight is crucial for better, more accurate space weather predictions.

During the last decade, some authors have numerically studied the propagation characteristics for a few typical observed CME events by 3-D MHD simulation, and the simulation results can reproduce time-dependent evolution of 3-D structures and be used to compare to real observations by the Large Angle and Spectrometric Coronagraph (LASCO) experiment, or STEREO, and Wind/ACE [e.g., *Wu et al.*, 1999; *Odstrcil et al.*, 2004, 2005; *Wu et al.*, 2007; *Shen et al.*, 2007, 2011; *Lugaz et al.*, 2007, 2009; *Manchester et al.*, 2004a, 2008; *Zhou et al.*, 2012]. For example, *Wu et al.* [1999] described the evolution of the January 1997 CME event by 2.5-D MHD model and compared the simulation results with Solar and Heliospheric Observatory (SOHO) and Wind data. *Odstrcil et al.* [2004] simulated 12 May 1997 CME event and provided a global heliospheric picture of transient disturbance interacting with solar wind stream structures. *Lugaz et al.* [2007] discussed the three-dimensional aspects of the propagation for the CMEs event with the Space Weather Modeling Framework (SWMF) and reproduced the shape of 24 November 2000 CMEs event as observed by the LASCO C3 coronograph and compared synthetic images with real observations from STEREO. *Manchester et al.* [2008] numerically modeled 28 October 2003 CME event with SWMF and found excellent agreement with both the general morphology and the quantitative brightness of the model CME with LASCO observations. *Shen et al.* [2011] investigated the dynamical interaction of 2000 April CME event with the background solar wind flow and the evolution of the physical parameters by 3-D time-dependent MHD simulation.

In the present paper, we choose 3 April 2010 CME event as our numerical study. The event was the first fast CME event toward Earth for the two STEREO spacecraft. The imagers on the two STEREO spacecraft (STEREO-A and STEREO-B) can continuously track this geo-effective CME from its inception at the surface of the Sun all the way to Earth. The wealth of data for this event provides us a good opportunity to study the propagation and the evolution of the CME. The paper is organized as follows. A brief description of observational properties of the CME event is given in section 2. The solar wind and CME initiation models are presented in sections 3 and 4, respectively. Section 5 gives the simulation results and analyzes the propagation characteristics of the halo CME event. Finally, we present a summary in section 6.

2. Observational Properties of the 3 April 2010 CME

The 3 April 2010 event was the first fast (800 km/s) ICME including a magnetic cloud observed by both the STEREO/HI instruments and a near-Earth spacecraft. At this time, the separation angles of STA and STB with Earth are 67° and 71°, respectively. The CME was an Earth-directed one, which was associated with a B7.4 X-ray flare recorded by GOES X-ray monitor from NOAA Active Region (AR) 11059 (S25W03). The flare was first seen in the extreme ultraviolet imaging telescope (EIT) on board SOHO between 09:14 UT and 10:00 UT associated with a faint EIT wave.

The STEREO observations suggest that the CME was traveling at a velocity of $\sim$ 1000 km/s close to the Sun and that it gradually decelerated to $\sim$ 700 km/s when the CME impacted the Earth. Consistent with these measurements, in situ instruments on board the NASA ACE spacecraft observed an interplanetary (IP) shock traveling with a solar wind velocity of $\sim$ 750 km/s at 7:51 UT on 5 April. The IP shock was followed by an IP coronal mass ejection (ICME), which caused an extended geomagnetic storm with minimum $Dst = -72$ nT on 5–7 April 2010 [*Xie et al.*, 2012]. The 3 April 2010 event has been studied by several authors [*Mostl et al.*, 2010; *Liu et al.*, 2011; *Wood et al.*, 2011; *Xie et al.*, 2012].

3. The Solar Wind Model

In this section we briefly present the solar wind model. The steady state solar wind used in our model is based on the model of *Zhou et al.* [2012], in which, the basic equations governing the evolution of the solar wind system are the modified MHD equations. This model can reproduce the solar wind background by means of an artificial heating/acceleration source term in the energy equation, which is given by

$$S_E = Q_0 \cdot \frac{1}{f_s} \exp(-r/L_Q), \tag{1}$$

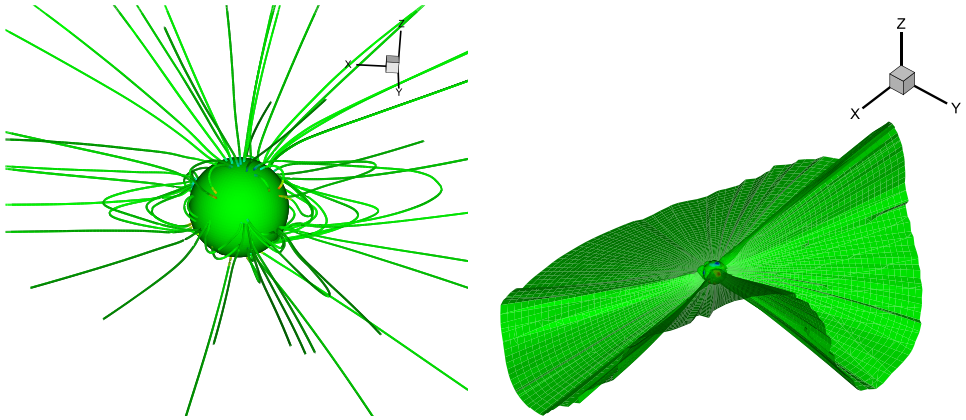

Figure 1. (a) Three-dimensional steady state magnetic field structure and (b) steady state current sheet in the solar corona domain.

where the constant value of Q_0 is set to be 0.5×10^{-6} J m^{-3} s^{-1}, and the decay length of heating L_Q is set to be 0.9 R_s. The expansion factor f_s is defined as $f_s = \left(\frac{R_s}{r}\right)^2 \frac{B_{R_s}}{B_r}$, where R_s and r are 1 solar radius and the distance from the solar center, and B_{R_s} and B_r are magnetic field strength at the solar surface and at r. For the specific heat ratio γ, similar to that of *Jacobs and Poedts* [2011], a variable polytropic index is used:

$$\gamma = \begin{cases} \gamma_0 & \text{if} \quad r < r_1, \\ \gamma_0 + (\gamma_1 - \gamma_0)\sin^2\left(\frac{\pi}{2}\frac{r-r_1}{r_2-r_1}\right) & \text{if} \quad r_1 \le r \le r_2, \\ \gamma_1 & \text{if} \quad r > r_2, \end{cases} \tag{2}$$

where the value of γ is smoothly varying between the value γ_0 close to the Sun, where $\gamma_0 = 1.2$ and its value, $\gamma_1 = 1.46$, that *Totten et al.* [1995] concluded from the analysis Helio 1 data as an average value for the polytropic index between 0.3 AU and 1 AU. The variation in γ takes place between the radial distances r_1 and r_2, where r_1 and r_2 are taken to be 1 R_s and 20 R_s, respectively.

The temperature and plasma density at the inner boundary are typically taken to be 1.5×10^6 K and 0.85×10^{-13} kg m^{-3}, respectively. The computational domain covers $-90° \le \theta \le 90°, 0° \le \phi \le 360°$, and 1 $R_s \le r \le 235$ R_s. Similar to that of *Zhou et al.* [2012], the quasi-steady solar wind is computed with the observed photospheric magnetic field and Parker's 1-D solar wind solution [*Parker*, 1963] as the initial values. For details of computing the solar wind background, please refer to the work of *Feng et al.* [2007, 2010].

Figure 1 shows the three-dimensional coronal field and heliospheric current sheet (HCS) structure. From the figure, we can easily see that the magnetic field and radial speed possess a typical characteristic of the rising phase. The coronal magnetic field shows a mixed dipole/quadrupole configuration with large tilt angle of the dipole. And the latitudinal extent of the HCS expands to higher latitudes, a north-south asymmetry appears around the heliospheric equator due to the quadrupole strength of the coronal field. Figure 2a shows the steady state solution in the solar equatorial plane. The result shows that the magnetic field generates the sector structure in interplanetary space. Figure 2b shows a cut through the ecliptic as well as along the meridional plane of E67, E0, and W71. The figure gives the information on how the solar wind speed is structured in IP space along the flank of the CME as viewed on STEREO-A, Earth, and STEREO-B meridional planes. We can find that there are significant differences in the speed distribution.

4. CME Initiation

The CME is initiated in an identical manner to the simple model described by *Zhou et al.* [2012]. In fact, there is no general consensus yet on the triggering mechanism for the CME, although a number of theoretical models have been proposed to explain its eruption and evolution near the Sun, e.g., the photospheric converging and shear motions [*Forbes et al.*, 1994; *Mikic and Linker*, 1994; *Antiochos et al.*, 1994], flux emergence [*Feynman and Martin*, 1995; *Chen and Shibata*, 2000], and flux cancellation [*Zhang et al.*, 2001]. Therefore, the model in this paper does not address the question of how such an energetic CME is initiated, but describes

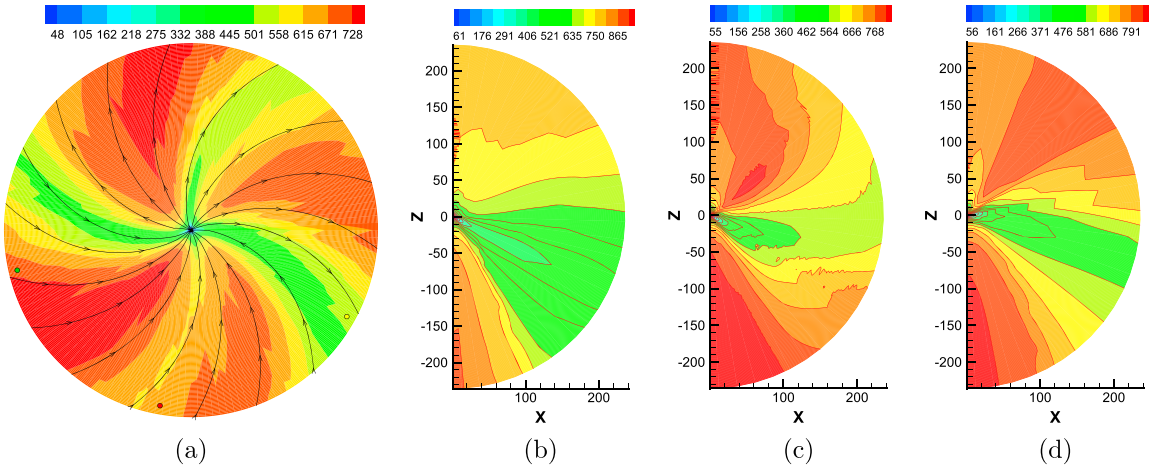

Figure 2. (a) Steady state solution in the solar equatorial plane. The black streamlines denote the magnetic field lines, the green, red, and yellow circles represent STEREO-A, Earth, and STEREO-B, respectively. (b–d) Steady state solution at the meridional plane of E67, E0, and W71, respectively. The color contours represent the radial speed (km/s).

the propagation of the CME from the low corona, the impact of the CME on the interplanetary medium, and the extreme conditions to which such a CME would subject the Earth's magnetosphere. The CME model is suggested in detail by *Zhou et al.* [2012], in which we have successfully simulated some important features of 4 November 1997 CME event. In the following, we briefly describe the CME initiation model.

The density, temperature, and radial velocity profile of the initial perturbation are defined as follows:

$$\begin{aligned} \rho &= \rho_{\text{wind}} + \rho_{\text{max}}(1 - a^2/a_{\text{cme}}^2) \\ T &= T_{\text{wind}} + T_{\text{max}}(1 - a^2/a_{\text{cme}}^2) \\ v_r &= v_{r_{\text{wind}}} + v_{\text{max}}(1 - a^2/a_{\text{cme}}^2) \end{aligned} \tag{3}$$

where a_{cme} is the radius of the plasmoid, a denotes the distance from the center of the plasmoid, and ρ_{wind}, $v_{r_{\text{wind}}}$, and T_{wind} are the density, radial velocity, and temperature of the solar wind background. ρ_{max}, v_{max}, and T_{max} are the maximum density, radial velocity, and temperature added on the solar wind background, respectively.

The magnetic field of the initial CME is assumed to take the form as that in *Zhou et al.* [2012] in local spherical coordinates $(r^\ell, \theta^\ell, \phi^\ell)$:

$$\begin{aligned} B_{r^\ell} &= (2B_0/\alpha r^\ell) j_1(\alpha r^\ell) \cos\theta^\ell \\ B_{\theta^\ell} &= -(B_0/\alpha r^\ell)[\sin(\alpha r^\ell) - j_1(\alpha r^\ell)] \sin\theta^\ell \\ B_{\phi^\ell} &= \pm B_0 j_1(\alpha r^\ell) \sin\theta^\ell \end{aligned} \tag{4}$$

where B_0 is a constant, and $\alpha = 4.493409458 a_{\text{cme}}^{-1}$ is the constant derived from the force-free condition of $\nabla \times \mathbf{B} = \alpha \mathbf{B}$ with the boundary condition of $B_{r^\ell} = 0$ at $r^\ell = a_{\text{cme}}$. The spherical Bessel function is $j_1(x)$, $j_1(x) = x^{-2}\sin x - x^{-1}\cos x$. The parameter α becomes negative for left-handed polarity.

In the simulation, we empirically choose the parameters of the CME model to match the simulated properties of the ICME reasonable well with in situ measurements at 1 AU. The CME is launched at 2.0 R_s at t = 09:20 UT, when the CME is first observed by EIT in the lower corona. The radius of the initial CME, a_{cme}, is 0.8 R_s. We assume ρ_{max} and T_{max} are 6 and 5 times larger than the value of the solar wind ambient at the center of the CME, respectively. The value of v_{max} is set to be 500 km/s. The maximal magnetic field strength B_0 is 5.0 G. We launch the CME at S25W03 to conform to the location of the flare/CME. In order to find a better agreement with the in situ interplanetary magnetic field (IMF) observations, we rotate the polar axis of the ejected spheromak toward the negative y axis direction, so that the polar axis is inclined about 20° from the negative y axis. The introduction of the plasmoid to the corona has added 6.93×10^{31} ergs of magnetic energy, 1.54×10^{30} ergs of kinetic, and 3.68×10^{31} ergs of thermal energy. The total energy (magnetic + kinetic + thermal energy) increase is 1.08×10^{32} ergs.

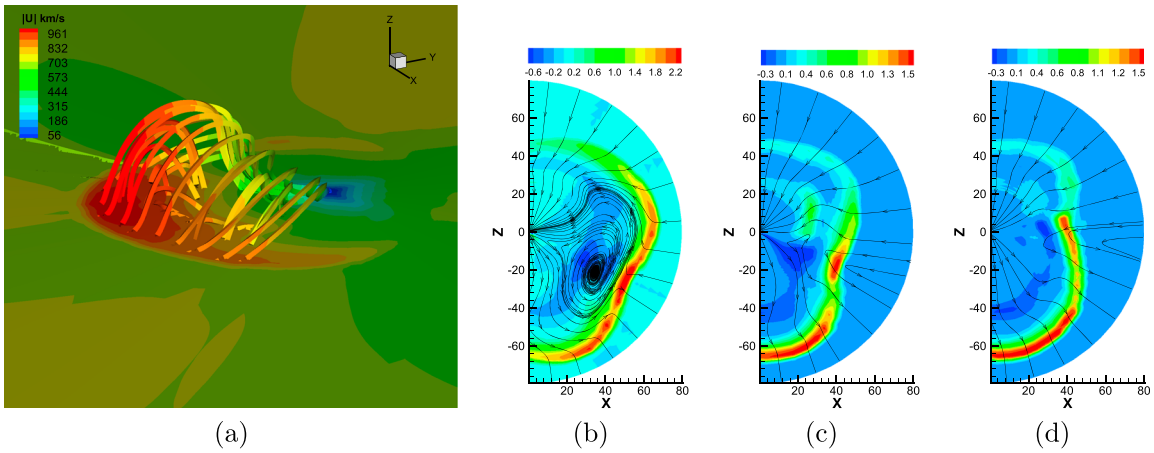

Figure 3. (a) A 3-D representation of the CME is shown at 10 h after initiation. The color code represents the velocity magnitude in the *x*-*y* equatorial plane. Field lines of the CME are shown in color to illustrate velocity magnitude. The Sun is shown with a green sphere. (b–d) Contour plots of the relative density distribution after 10.0 h at E67, E0, and W71 meridional planes, respectively. The black lines represent the magnetic field. The relative density is defined as follows: $\overline{\rho} = (\rho - \rho_{\text{wind}})/\rho_{\text{wind}}$.

5. Simulation Results

In this section, we perform a comprehensive study on the evolution and propagation of the 3 April 2010 CME/shock by comparing the remote sensing observations of STEREO in the corona, the in situ observations of Wind, with the simulation results of 3-D SIP-CESE MHD model, and analyze several propagation characteristics of the CME.

5.1. The Morphology and Propagation of the CME

A three-dimensional view together with a radial velocity distribution in $y = 0$ plane at 10 h after the eruption of the CME is shown in Figure 3a. The corresponding 2-D meridional slices at E67, E0, and W71 with false color images of the relative density is depicted in Figures 3b–3d, respectively, upon which black lines represent the magnetic field. At this time, the CME front has reached 58 R_s. The maximum radial velocity of the CME is approximately 770 km/s. From Figure 3b, we find that the front of the flux rope begins to flatten, since the flux rope is stalled by the dense plasma sheet around the HCS. This phenomenon has been found in earlier work [*Manchester et al.*, 2004a; *Zhou et al.*, 2012]. However, the flux rope does not expand to E67 and W71 meridional planes, as seen from Figures 3c and 3d. The distribution of the relative density exhibits a concave outward shape in Figures 3b–3d due to the HCS largely distorting the shock front. The large-scale concave feature of the shock front is consistent with previous simulations and observations [*Odstrcil et al.*, 1996; *Manchester et al.*, 2004a].

In Figure 4, we produce synthetic line-of-sight differential images of CME observed from the STA/STB by integrating the simulated density and compare observed and synthetic images. The figures of the first and third columns are the CME running difference images for the CME from STA/STB, respectively. The second and fourth columns show the corresponding synthetic images. The first and second rows are from STA/STB COR1 and COR2, respectively. From the first and second rows, we can see that the simulated images capture some features of the event such as the bright outer loop but unfortunately miss the bright core of density structure, where three-part structure was observed in COR1 and COR2. This might be due to the simple CME model used here. In the third row, we compare synthetic images of the CME in the heliosphere from the point of view of STA/STB with real images. We can see that there is a good agreement between the overall shape and position of the CME in real and synthetic images of the CME observed. In particular, the concave outward density structure is well reproduced. However, the size of CME in the synthetic image is larger than the real one. This might be due to an overexpansion of the simulated CME owing to its initiation setup.

5.2. Properties of the CME at 1 AU

Figure 5 shows the 3-D structure of the distorted flux rope and its interaction with the solar wind at $t = 43$ h, when the front of the CME reaches 1 AU. Here the front of the CME is shown as an isosurface of $\overline{\rho} = 2\rho_{\text{wind}}$, and false color representations of velocity magnitude cover the isosurface. The yellow sphere is positioned at the Earth and has a radius of 5 R_s. It is clear that the front of the CME already arrives at Earth at this

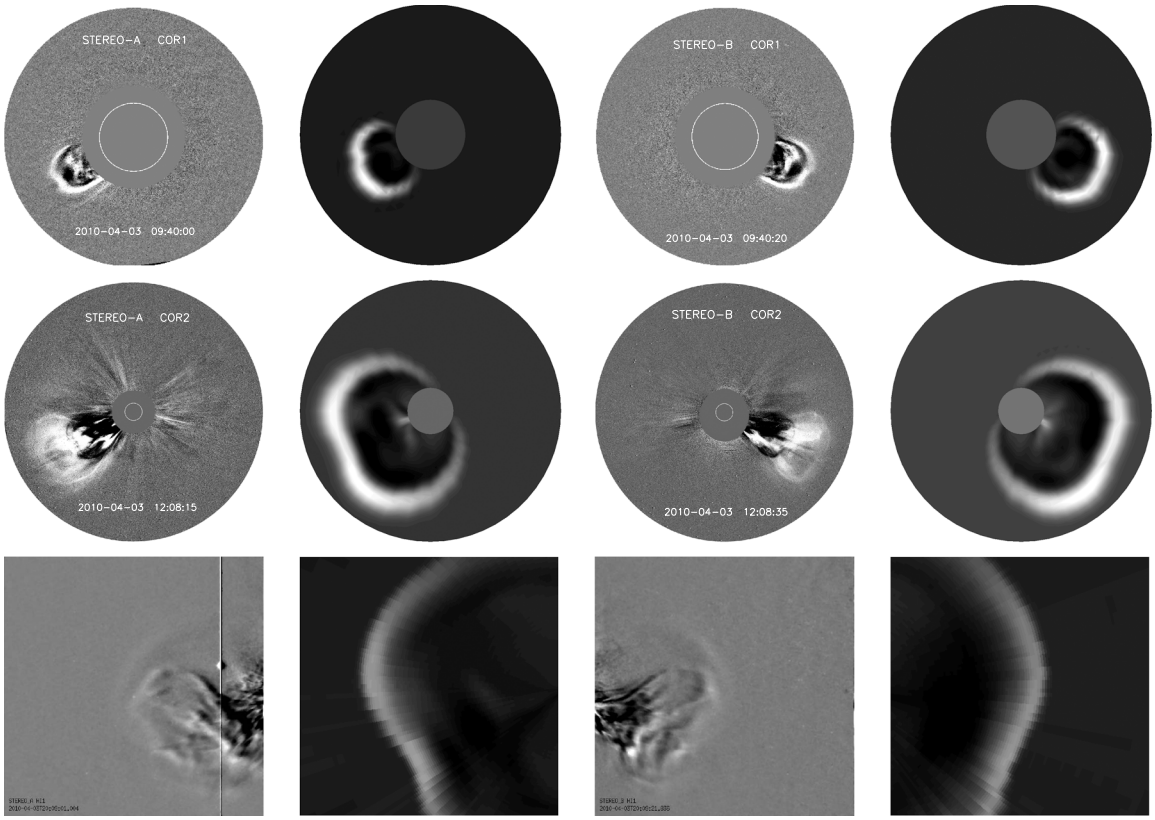

Figure 4. Comparison of (first and third columns) synthetic image and (second and fourth columns) real STEREO images. The three rows show images from COR1, COR2, and HI1, respectively. The first and third columns display images from STA and STB, respectively.

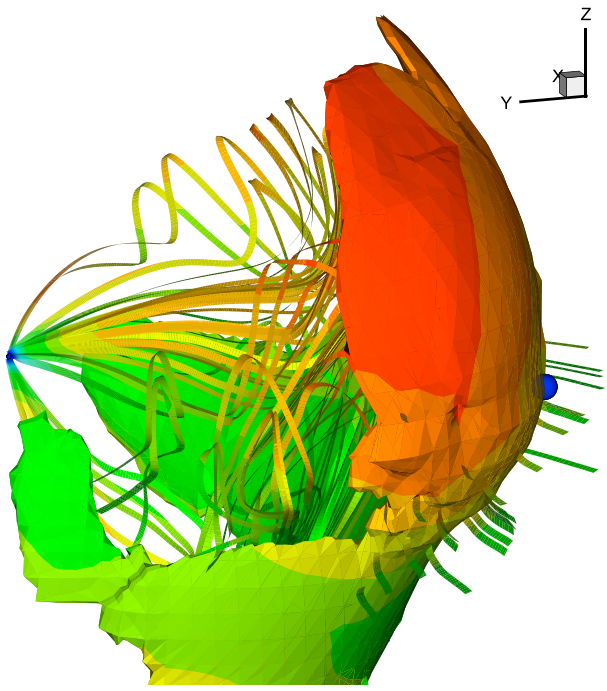

Figure 5. A 3-D representation of the CME is shown at 43 h after initiation. The color code represents the velocity magnitude. A 3-D colored isosurface of $\overline{\rho} = 2\rho_{\text{wind}}$ is drawn. The blue sphere shows the position of the Earth and has a radius of 5 R_s.

time from the figure. The solar wind magnetic field is shown in color to illustrate the velocity magnitude. These lines fully characterize field line topology near 1 AU. From the figure, we find that the magnetic field structure evolves to a crescent shape near 1 AU.

Figure 6 gives plasma parameters of the simulation results as a function of time at 1 AU (solid lines) and makes a comparison with in situ measurements of Wind observation between 4 and 9 April (dashed lines). From this figure, we find that our simulation successfully reproduces the main features of ICME, for example, the similar curves of the plasma density and velocity, the behaviors of magnetic field: in particular an increase in the magnetic field magnitude, B_x and southward B_z, and the large-scale smooth magnetic field rotation.

From Figure 6, we find that the IP shock arrives at Wind on 5 April at 07:58 UT. Our model predicts the shock arrival at Earth at about 05:50 UT on 5 April, with an error

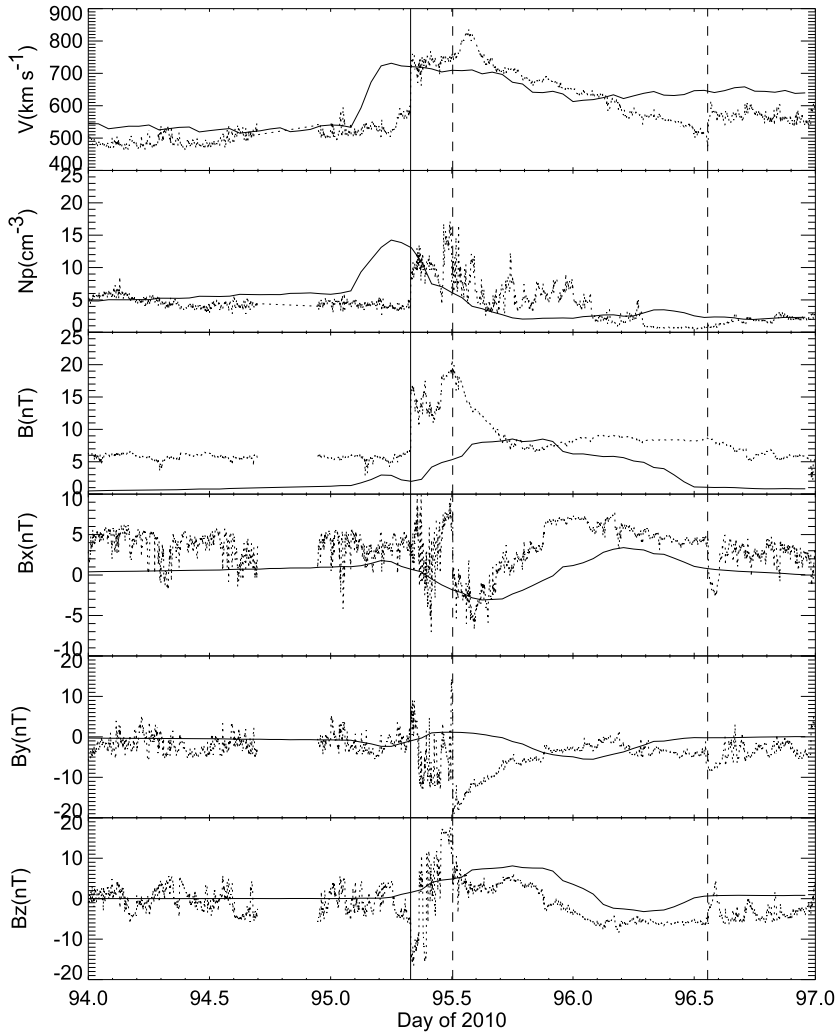

Figure 6. Comparison between the in situ data obtained by the Wind spacecraft and our simulation during the 3 April 2010 event. (top to bottom) Flow velocity, number density, magnetic field, and three components of magnetic field in geocentric solar ecliptic coordinates. The vertical solid line indicates the time of the ICME-driven shock. The vertical dashed line indicates the starting and ending time of the magnetic cloud. The simulation results at the Earth are shown by the solid lines. The Wind observations are shown by the dotted lines.

of 2 h compared to the Wind shock arrival time (SAT). So the model provides a good prediction of the SAT for this event. The shock is followed by an ICME from 5 April at 12:00 UT to 6 April at 17:00 UT. The observed ICME has the low proton temperature, smooth and strong magnetic field, and declining speed profile. For the magnetic field, we find that the simulated and measured profiles at 1 AU are very similar, in particular, for B_x and B_z components and the large-scale smooth magnetic field rotation. From the computed B_z at 1 AU shown in Figure 6, we find that the field turns northward at ~ 10:00 UT on 5 April 2010 for 17.5 h, reaching a maximum 8 nT. Then the magnetic field smoothly rotates southward reaching a minimum −3.3 nT, lasting more than 11 h. The north-south rotation of this magnetic field is mainly due to the passage through the helical field of the CME suggested by *Wu et al.* [1999]. The magnetic field shown in Figure 6 has a prolonged negative (southward) component spanning the ICME. A southward magnetic field can reconnect with geomagnetic fields and thus is a key factor in producing geomagnetic storms [*Dungey*, 1961; *Gosling et al.*, 1991]. But the simulated magnetic field at 1 AU is smaller than that of the observed magnetic cloud. This may be attributed to the small background magnetic field caused by the imperfectness of potential field source surface model and the coarse grid resolution in IP space.

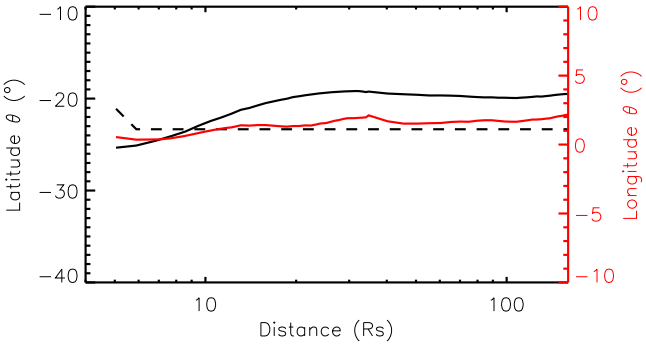

Figure 7. Propagation trajectory of $PATH_{CME}$'s latitude (black solid line) and longitude (red solid line). The dotted line shows the position angles of HCS at different heights.

5.3. Characteristics of the CME

The interplanetary observations suggest that the ICME encountered the Earth, while it missed the STEREO A and B spacecraft. In the following, we will study several factors that affect the probability of the CME's encounter with the spacecraft, such as the speed, span angle, and the deflection. This is also an interesting topic in predicting whether a CME will encounter the Earth.

5.3.1. Analysis of the Evolution Path

With the help of simulation results, we can derive the CME trajectory from near the Sun all the way to 1 AU during its outward propagation. In order to quantitatively study the propagation trajectory of CME, we define the 3-D centroid of CME as $PATH_{CME}$ (including CME central distance from the Sun, CME central latitude, and CME central longitude) by the relative mass:

$$\mathrm{PATH}_{\mathrm{CME}}(r,\theta,\phi)=\frac{\sum_{ijk}\bar{\rho}_{ijk}(r_i,\theta_j,\phi_k)r_i\sin\theta_j\mathrm{d}r_i\mathrm{d}\theta_j\mathrm{d}\phi_k}{\sum_{ijk}\bar{\rho}_{ijk}r_i\sin\theta_j\mathrm{d}r_i\mathrm{d}\theta_j\mathrm{d}\phi_k}$$

where $\bar{\rho}$ denotes the relative density (identified by the 20% enhancement of the density, i.e., $\bar{\rho}=1.2\rho_{\mathrm{wind}}$), and the indices i, j, and k run over all grid points in the radial, meridional, and azimuthal directions, respectively.

Figure 7 shows the propagation trajectory of $PATH_{CME}$'s latitude and longitude with its distance. The dotted line in the figure shows the position angles of HCS at different heights. The black and red solid lines show the variation of $PATH_{CME}$'s latitude and longitude away from the Sun-Earth line, respectively. From the figure, we find that the CME shows a deflection of about 5° toward the solar equator during its outward propagation from the corona to about 20 R_s, this is due to the effect of the magnetic density gradient. The equatorward deflection propagation of the CME event during its outward propagation has been studied by many researchers [e.g., *Cremades and Bothmer*, 2004; *Kilpua et al.*, 2009b; *Gui et al.*, 2011; *Kay et al.*, 2013]. Then the CME almost propagates along the HCS in the latitudinal direction in interplanetary space. And the result also displays that the CME does not deflect in longitudinal direction, since the $PATH_{CME}$'s longitude away from the Sun-Earth line only shows about 2° variation during its outward propagation from the corona to about 1 AU.

Figure 5.3.1 shows the simulated global view of the relative density in the equatorial plane at different instants. The red circle in the figure shows the position of the Earth. From this figure, we find that the CME almost propagates along the Sun-Earth line. There is almost no pronounced westward or eastward deflection of the CME during its outward propagation because of the little speed difference between the CME and the solar wind background. This is consistent with the observational analysis of the deflection of CMEs' propagation in interplanetary space by *Wang et al.* [2004]. The angle between the initial CME radial direction and the IMF at 1 AU calculated from the simulated solar wind background results is 36°; the Sun rotates about 33° from the east to west when the magnetic cloud center arrives at the Earth. This means that the CME almost moves outward along the Parker spiral interplanetary magnetic field. An asymmetry structure of the CME is clearly seen in heliolongitude as it passes into nonuniform solar wind ambient, and the asymmetry of the CME in heliolatitude can also be clearly seen from Figure 5.3.1.

5.3.2. The Spread Angle

In the following, we will study the evolution of the spread angle of the corresponding CME on the Sun-Earth meridional plane. Because the wing of the CME can encounter the spacecraft, even if the center of the CME misses it. If the Earth is near the spacecraft, this means that the wing of the CME can interact with the magnetosphere and may create a severe geomagnetic storm. We define the spread angle by means of the relative density plots on which we determine the contour where the relative density $\bar{\rho}$ is 1 (i.e., $\bar{\rho}=2\rho_{\mathrm{wind}}$). The spread angle of this contour measured from the solar center is defined as the spread angle of the CME.

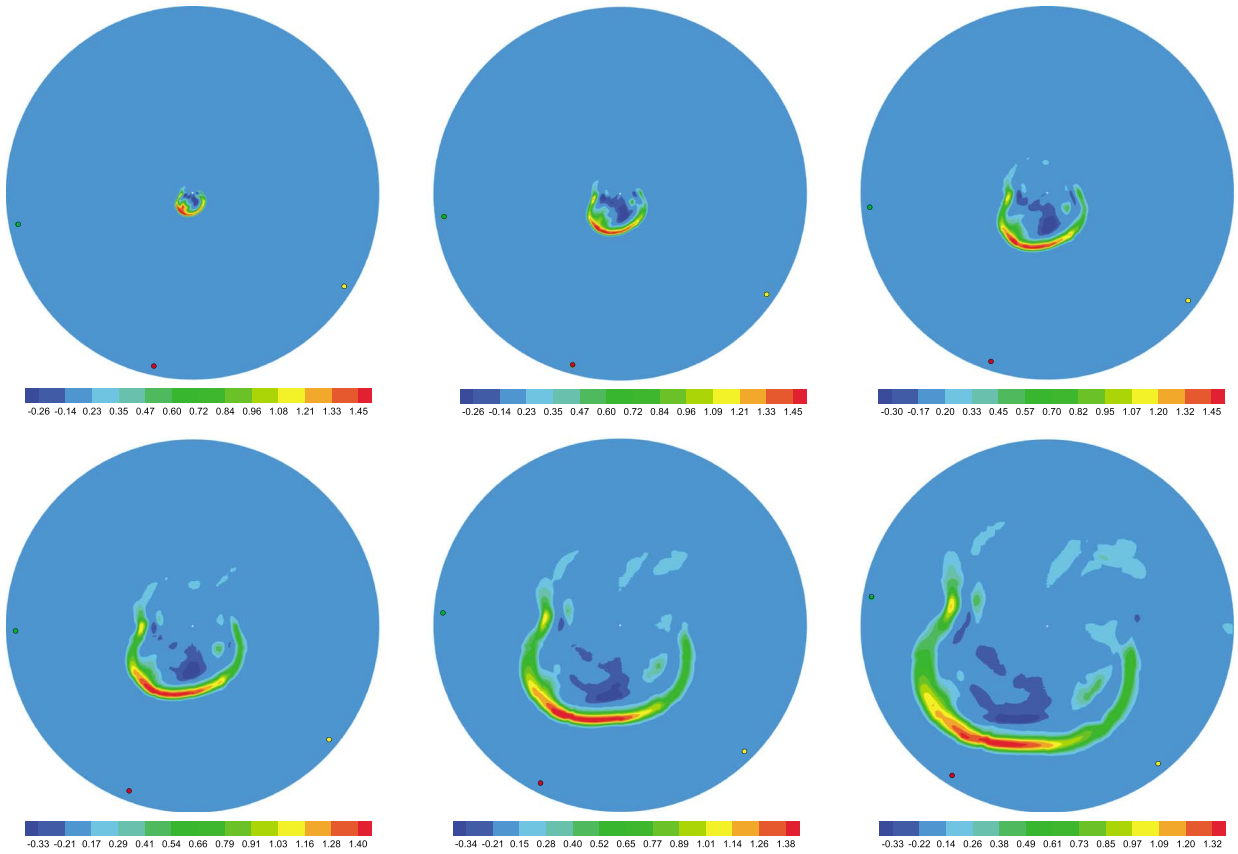

Figure 8. The simulated profiles of the relative density in the *x-y* azimuthal plane at (a) 5 h, (b) 10 h, (c) 15 h, (d) 20 h, (e) 30 h, and (f) 40 h. The red circle shows the position of the Earth, and the yellow and green circles show the position of STEREO A and B, respectively.

Though this definition is rather simple, at least it is based on mathematics and can reflect the propagation characteristics of the CME to some extent. Figure 9 shows the evolution of the spread angle (black line) and meridional width (red line) in time. The spread angle quickly evolves to 150° just 1.5 h after the CME initiation, at which time the CME center is at a distance of 10 R_s. The quick increase of spread angle during the first 1.5 h of the CME's propagation is clearly correlated with the rapid expansion due to the initial high speed, pressure, and plasma density plasmoid imposed on the solar wind ambient. During the same time, the CME's velocity rapidly decelerates (see Figure 11a). From the evolution of the meridional width (red line) in Figure 9, we find that CME keeps constantly expanding when going outward. However, the CME's spread angle varies slightly from 150° to 135° between 1.5 and 5 h. This may be due to the combined interaction of the CME with the background solar wind. As the CME propagates beyond 10 R_s (after 1.5 h), the solar wind becomes dominant, and magnetic fields decrease quickly. The ambient solar wind may largely distort the shock front. The dense plasma in the HCS recess the center of the CME, and the extremities of the CME at high latitude are swept radially forward by the fast solar wind—thus resulting in a concave outward in the shock front and the variety of the CME spread angle. After 7 h, the spread angle remains almost around 140°. This means that the CME

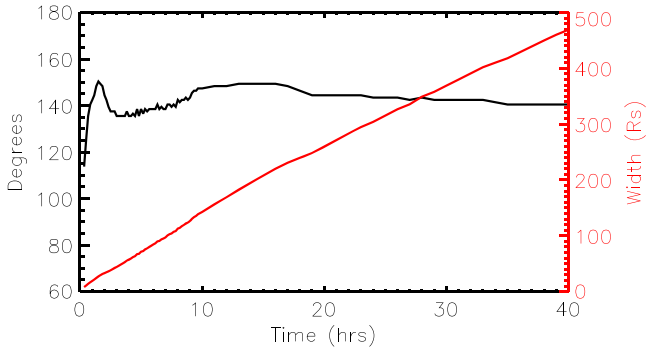

Figure 9. The evolution of the spread angle (black) and meridional width (red) of the CME in time.

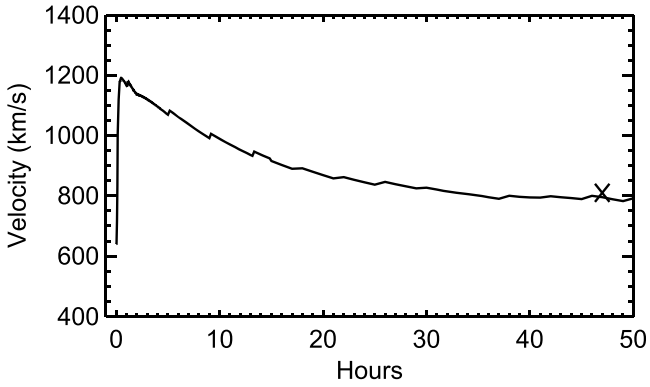

Figure 10. Time-velocity profile along the Sun-Earth line; the cross marks the Wind observation data.

continues to expand during its propagating outward in IP space. The CME's expansion should continue even if it passes the spacecraft until a pressure equilibrium is established. This dynamic behavior has been found in previous works [e.g., *Gosling et al.*, 1998; *Wang et al.*, 2005]. By studying the evolution of the radial width of the ICMEs (up to ~ 5 AU), these authors found that ICMEs expanded and the average width of ICMEs increased as traveling outward, since the internal pressure was generally larger than that of the surrounding wind.

5.3.3. Velocity

One of the central points of space weather forecasting is the prediction of ICME arrival at Earth. We know that the CME velocity is a key factor affecting its arrival time. Figure 10 shows the CME's velocity along the Sun-Earth line versus time. From the figure, we find that the CME rapidly accelerates to about 1200 km/s just 0.5 h after the CME initiation, then the speed begins to decelerate to about 800 km/s until the CME arrives at the Earth. By comparison with the Wind observation data (marked by the cross in Figure 10), we find that the simulation result and observation result are almost the same. *Xie et al.* [2012] gave three approximations of the velocity along the Sun-Earth line by observation data and approved that the Harmonic Mean method gave the smallest error, and our result is similar to that by the Harmonic Mean method. This implies the effectiveness of the numerical result.

In the following, we see the velocity of the CME's center (Figure 11a). From the figure, we find that the speed of the CME's center rapidly accelerates to about 1600 km/s just several minutes after the CME initiation due to the imposed initial pressure imbalance. Then the speed quickly begins to decelerate to about 936 km/s at 4 h after the CME initiation, when the CME center already reaches 24 R_s in interplanetary space. The rapid deceleration with a relatively short time is associated with the interactions with the solar wind ambient due to the large drag by the background medium and the quick expansion of the CME (see Figure 9). Figure 11b shows the velocity of the center as a function of distance as a solid line. We find that the variety of the velocity along heliocentric distance within 24 R_s is similar to the empirical relationship (dashed line in Figure 11b) put forth by *Sheeley et al.* [1999] and simulated by *Manchester et al.* [2004b]. *Sheeley et al.* [1999] described the deceleration of fast halo CMEs observed with LASCO, by giving the following empirical relationship:

$$r(t) = r_0 + v_1 t + (1 - e^{-t/\tau})(v_0 - v_1)\tau \tag{5}$$

$$v(t) = v_1 + (v_0 - v_1)e^{-t/\tau} \tag{6}$$

For our CME modeled, we find $r_0 = 3.0\,R_s$, $v_0 = 1503$ km/s, and $v_1 = 936$ km/s and $\tau = 1.0$ h gives a close fit to our numerical simulation. After 4 h, the speed keeps on slowly decreasing to 658 km/s through

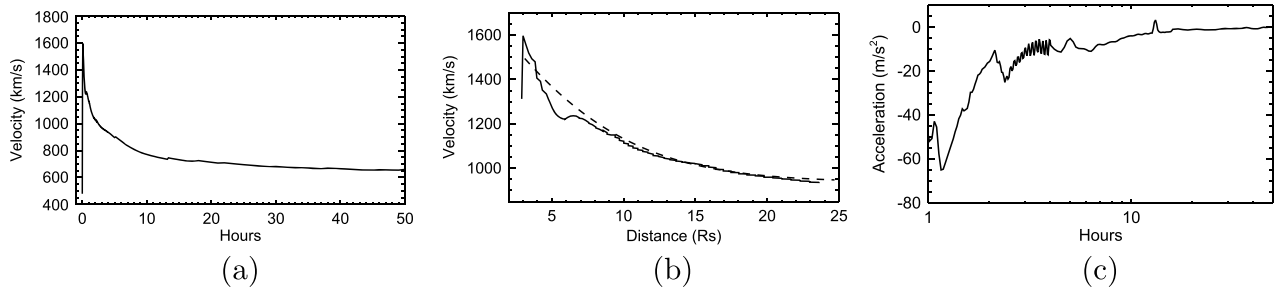

Figure 11. (a) Time-velocity profile, (b) velocity-distance profile, and (c) time-acceleration profile along the center of CME. The dashed line in Figure 11b shows an empirical relationship expressed by an exponential decay in velocity that closely approximate the evolution of the model CME [*Sheeley et al.*, 1999].

the interaction with the solar wind background till the IP shock arrives at 1 AU. The result verifies that the velocity profile of the CME's center includes three phases: an impulsive acceleration near the corona, a faster deceleration phase, and then a more gradual deceleration phase during the fast CME event propagation. In order to better demonstrate the variety of the velocity, the corresponding acceleration along the CME's center from 1 h to 50 h is shown in Figure 11c. We can find that the acceleration along the CME's center is about -55 m/s^2 at 1 h; this value is very similar to that obtained by the acceleration $a(t) = -(v_0 - v_1)/\tau e^{-t/\tau}$ for the fast CME event in *Sheeley et al.* [1999]. Then it rapidly rises to -10 m/s^2 at 4 h after the CME initiation and slowly rises to about -0.5 m/s^2 when the shock arrives at 1 AU. During the time, the speed dropped from 936 km/s to 658 km/s in about 39.5 h, the corresponding acceleration is -1.95 m/s^2, which is consistent with the IP acceleration $a = 2.193 - 0.0054u$ from *Gopalswamy et al.* [2005] empirical shock arrival (ESA) model, where u is the CME speed. For $u = 750$ km/s; $a = -1.857$ m/s^2.

6. Conclusions

In this paper, by using a three-dimensional numerical MHD simulation, we have investigated the corona and heliospheric evolution of 3 April 2010 CME. The CME event (observed by both STEREO A and B throughout the whole Sun-Earth space) with the largest, fastest ICME at 1 AU since the 13 December 2006 event provides us a good opportunity to study its propagation and evolution from the Sun up to 1 AU.

Using the 3-D simulation results of the CME in the solar corona and in the heliosphere, we produce the synthetic coronagraphic images, which are compared with the real observed images. We find that the results can successfully reproduce the observations in the STEREO A and B field of view. Then we follow the propagation of the CME from the corona to 1 AU and examine the time evolution of plasma properties. By comparing the simulation results with the Wind-measured data, we find that the simulation results can successfully generate many basic structures of the in situ measurement: such as the similar curves of the plasma density and velocity, an increase in the magnetic field magnitude, the large-scale smooth magnetic field rotation, and prolonged southward IMF (a well-known source of magnetic storms). Finally, we analyze in detail the propagation velocity, the spread angle, the trajectory of CME. The speed of the CME rapidly increases from near the Sun, then decreases due to interaction with the solar wind ambient. The spread angle of the CME quickly increases due to lateral material expansion by the pressure gradients within the solar wind background, then the expansion decreases with distance and ends until a pressure equilibrium is established. We also study the CME deflection and find that the CME shows a deflection of about 5° toward the solar equator during its outward propagation from the corona to about 20 R_s, then the CME almost propagates along the HCS in the latitudinal direction in interplanetary space. The CME almost does not deflects in the longitudinal direction during its propagation from the Sun to 1 AU. In addition to the CME's propagation characteristics, such as its propagation velocity, shape, and trajectory, we will analyze its energy transfer and mass and study more typical CME events in detail. The study of these topics will help us to further understand CME's propagation process and enhance our future space weather forecasts.

Acknowledgments

The work is jointly supported by the National Basic Research Program (973 program) under grant 2012CB825601, the Knowledge Innovation Program of the Chinese Academy of Sciences (KZZD-EW-01-4), the National Natural Science Foundation of China (41231068, 41031066, 41374176, 41174150, 41274179, and 41274192), and the Specialized Research Fund for State Key Laboratories. The numerical calculation has been completed on our SIGMA Cluster computing system. The Wilcox Solar Observatory data used in this study were obtained via the Web site http://wso.stanford.edu at 2009:05:06_17:15:30 PDT courtesy of J.T. Hoeksema. The Wilcox Solar Observatory is currently supported by NASA. We also thank OmniWeb, http://omniweb.gsfc.nasa.gov/, from which we downloaded the hourly average solar wind data by Wind.

Yuming Wang thanks the reviewers for their assistance in evaluating this paper.

References

Antiochos, S. K., R. B. Dahlburg, and J. A. Klimchuk (1994), The magnetic field of solar prominences, *Astrophys. J.*, *420*, L41–L44, doi:10.1086/187158.

Chen, P. F., and K. Shibata (2000), An emerging flux trigger mechanism for coronal mass ejections, *Astrophys. J.*, *545*, 524–531, doi:10.1086/317803.

Cremades, H., and V. Bothmer (2004), On the three-dimensional configuration of coronal mass ejections, *Astron. Astrophys.*, *422*, 307–322, doi:10.1051/0004-6361:20035776.

Davies, J. A., R. A. Harrison, A. P. Rouillard, N. R. Sheeley, C. H. Perry, D. Bewsher, C. J. Davis, C. J. Eyles, S. R. Crothers, and D. S. Brown (2009), A synoptic view of solar transient evolution in the inner heliosphere using the heliospheric imagers on STEREO, *Geophys. Res. Lett.*, *36*, L02102, doi:10.1029/2008GL036182.

Domingo, V., B. Fleck, and A. Poland (1995), The SOHO mission: An overview, *Sol. Phys.*, *162*(1-2), 1–37, doi:10.1007/BF00733425.

Dungey, J. W. (1961), Interplanetary magnetic field and the auroral zones, *Phys. Rev. Lett.*, *6*, 47–48, doi:10.1103/PhysRevLett.6.47.

Eyles, C., et al. (2009), The heliospheric imagers onboard the STEREO mission, *Sol. Phys.*, *254*(2), 387–445, doi:10.1007/s11207-008-9299-0.

Feng, X., Y. Zhou, and S. T. Wu (2007), A novel numerical implementation for solar wind modeling by the modified conservation element/solution element method, *Astrophys. J.*, *655*, 1110–1126, doi:10.1086/510121.

Feng, X., L. Yang, C. Xiang, S. T. Wu, Y. Zhou, and D. Zhong (2010), Three-dimensional solar WIND modeling from the sun to Earth by a SIP-CESE MHD model with a six-component grid, *Astrophys. J.*, *723*, 300–319, doi:10.1088/0004-637X/723/1/300.

Feynman, J., and S. F. Martin (1995), The initiation of coronal mass ejections by newly emerging magnetic flux, *J. Geophys. Res.*, *100*, 3355–3367, doi:10.1029/94JA02591.

Forbes, T. G., E. R. Priest, and P. A. Isenberg (1994), On the maximum energy release in flux-rope models of eruptive flares, *Sol. Phys.*, *150*, 245–266, doi:10.1007/BF00712888.

Gosling, J. T., D. J. McComas, J. L. Phillips, and S. J. Bame (1991), Geomagnetic activity associated with Earth passage of interplanetary shock disturbances and coronal mass ejections, *J. Geophys. Res.*, *96*, 7831–7839, doi:10.1029/91JA00316.

Gopalswamy, N., A. Lara, P. K. Manoharan, and R. A. Howard (2005), An empirical model to predict the 1-AU arrival of interplanetary shocks, *Adv. Space Res.*, *36*, 2289–2294, doi:10.1016/j.asr.2004.07.014.

Gosling, J. T., P. Riley, D. J. McComas, and V. J. Pizzo (1998), Overexpanding coronal mass ejections at high heliographic latitudes: Observations and simulations, *J. Geophys. Res.*, *103*, 1941–1954, doi:10.1029/97JA01304.

Gui, B., C. Shen, Y. Wang, P. Ye, J. Liu, S. Wang, and X. Zhao (2011), Quantitative analysis of CME deflections in the corona, *Sol. Phys.*, *271*, 111–139, doi:10.1007/s11207-011-9791-9.

Hundhausen, A. J. (1987), The origin and propagation of coronal mass ejections (R), in *Proceedings of the Sixth International Solar Wind Conference*, edited by V. J. Pizzo, T. Holzer, and D. G. Sime, pp. 181, Natl. Cent. for Atmos. Res., Boulder, Colo.

Jacobs, C., and S. Poedts (2011), A polytropic model for the solar wind, *Adv. Space Res.*, *48*, 1958–1966, doi:10.1016/j.asr.2011.08.015.

Kaiser, M., T. Kucera, J. Davila, O. St. Cyr, M. Guhathakurta, and E. Christian (2008), The STEREO mission: An introduction, in *The STEREO Mission*, edited by C. Russell, pp. 5–16, Springer, New York, doi:10.1007/978-0-387-09649-0-2.

Kay, C., M. Opher, and R. M. Evans (2013), Forecasting a coronal mass ejection's altered trajectory: ForeCAT, *Astrophys. J.*, *775*(1), 5.

Kilpua, E., et al. (2009a), Multispacecraft observations of magnetic clouds and their solar origins between 19 and 23 May 2007, *Sol. Phys.*, *254*(2), 325–344, doi:10.1007/s11207-008-9300-y.

Kilpua, E. K. J., J. Pomoell, A. Vourlidas, R. Vainio, J. Luhmann, Y. Li, P. Schroeder, A. B. Galvin, and K. Simunac (2009b), STEREO observations of interplanetary coronal mass ejections and prominence deflection during solar minimum period, *Ann. Geophys.*, *27*, 4491–4503, doi:10.5194/angeo-27-4491-2009.

Lee, C., C. Arge, D. Odstrcil, G. Millward, V. Pizzo, J. Quinn, and C. Henney (2013), Ensemble modeling of CME propagation, *Sol. Phys.*, *285*(1–2), 349–368, doi:10.1007/s11207-012-9980-1.

Liu, Y., J. A. Davies, J. G. Luhmann, A. Vourlidas, S. D. Bale, and R. P. Lin (2010), Geometric triangulation of imaging observations to track coronal mass ejections continuously out to 1 AU, *Astrophys. J. Lett.*, *710*(1), L82.

Liu, Y., J. G. Luhmann, S. D. Bale, and R. P. Lin (2011), Solar source and heliospheric consequences of the 2010 April 3 coronal mass ejection: A comprehensive view, *Astrophys. J.*, *734*(2), 84.

Liu, Y. D., J. G. Luhmann, N. Lugaz, C. Mostl, J. A. Davies, S. D. Bale, and R. P. Lin (2013), On Sun-to-Earth propagation of coronal mass ejections, *Astrophys. J.*, *769*(1), 45.

Lugaz, N., W. B. Manchester IV, I. I. Roussev, G. Tóth, and T. I. Gombosi (2007), Numerical investigation of the homologous coronal mass ejection events from active region 9236, *Astrophys. J.*, *659*, 788–800, doi:10.1086/512005.

Lugaz, N., A. Vourlidas, I. I. Roussev, and H. Morgan (2009), Solar-terrestrial simulation in the STEREO era: The 24-25 January 2007 eruptions, *Sol. Phys.*, *256*, 269–284, doi:10.1007/s11207-009-9339-4.

Manchester, W. B., T. I. Gombosi, I. Roussev, A. Ridley, D. L. de Zeeuw, I. V. Sokolov, K. G. Powell, and G. Tóth (2004a), Modeling a space weather event from the Sun to the Earth: CME generation and interplanetary propagation, *J. Geophys. Res.*, *109*, A02107, doi:10.1029/2003JA010150.

Manchester, W. B., T. I. Gombosi, I. Roussev, D. L. de Zeeuw, I. V. Sokolov, K. G. Powell, G. Tóth, and M. Opher (2004b), Three-dimensional MHD simulation of a flux rope driven CME, *J. Geophys. Res.*, *109*, A01102, doi:10.1029/2002JA009672.

Manchester, W. B., IV, A. Vourlidas, G. Tóth, N. Lugaz, I. I. Roussev, I. V. Sokolov, T. I. Gombosi, D. L. De Zeeuw, and M. Opher (2008), Three-dimensional MHD simulation of the 2003 October 28 coronal mass ejection: Comparison with LASCO coronagraph observations, *Astrophys. J.*, *684*, 1448–1460, doi:10.1086/590231.

Mikic, Z., and J. A. Linker (1994), Disruption of coronal magnetic field arcades, *Astrophys. J.*, *430*, 898–912, doi:10.1086/174460.

Mostl, C., C. Farrugia, H. Biernat, M. Leitner, E. Kilpua, A. Galvin, and J. Luhmann (2009), Optimized Grad-Shafranov reconstruction of a magnetic cloud using STEREO-Wind observations, *Sol. Phys.*, *256*(1-2), 427–441, doi:10.1007/s11207-009-9360-7.

Mostl, C., M. Temmer, T. Rollett, C. J. Farrugia, Y. Liu, A. M. Veronig, M. Leitner, A. B. Galvin, and H. K. Biernat (2010), STEREO and Wind observations of a fast ICME flank triggering a prolonged geomagnetic storm on 5–7 April 2010, *Geophys. Res. Lett.*, *37*, L24103, doi:10.1029/2010GL045175.

Odstrcil, D., M. Dryer, and Z. Smith (1996), Propagation of an interplanetary shock along the heliospheric plasma sheet, *J. Geophys. Res.*, *101*(A9), 19,973–19,986, doi:10.1029/96JA00479.

Odstrcil, D., P. Riley, and X. P. Zhao (2004), Numerical simulation of the 12 May 1997 interplanetary CME event, *J. Geophys. Res.*, *109*, A02116, doi:10.1029/2003JA010135.

Odstrcil, D., V. J. Pizzo, and C. N. Arge (2005), Propagation of the 12 May 1997 interplanetary coronal mass ejection in evolving solar wind structures, *J. Geophys. Res.*, *110*, A02106, doi:10.1029/2004JA010745.

Parker, E. N. (1963), *Interplanetary Dynamical Processes*, Interscience Publishers, New York.

Prise, A., L. Harra, S. Matthews, D. Long, and A. Aylward (2014), An investigation of the CME of 3 November 2011 and its associated widespread solar energetic particle event, *Sol. Phys.*, *289*(5), 1731–1744, doi:10.1007/s11207-013-0435-0.

Sheeley, N. R., J. H. Walters, Y.-M. Wang, and R. A. Howard (1999), Continuous tracking of coronal outflows: Two kinds of coronal mass ejections, *J. Geophys. Res.*, *104*(A11), 24,739–24,767, doi:10.1029/1999JA900308.

Shen, F., X. Feng, S. T. Wu, and C. Xiang (2007), Three-dimensional MHD simulation of CMEs in three-dimensional background solar wind with the self-consistent structure on the source surface as input: Numerical simulation of the January 1997 Sun-Earth connection event, *J. Geophys. Res.*, *112*, A06109, doi:10.1029/2006JA012164.

Shen, F., X. S. Feng, S. T. Wu, C. Q. Xiang, and W. B. Song (2011), Three-dimensional MHD simulation of the evolution of the April 2000 CME event and its induced shocks using a magnetized plasma blob model, *J. Geophys. Res.*, *116*, A04102, doi:10.1029/2010JA015809.

Totten, T. L., J. W. Freeman, and S. Arya (1995), An empirical determination of the polytropic index for the free-streaming solar wind using HELIOS 1 data, *J. Geophys. Res.*, *100*, 13–17, doi:10.1029/94JA02420.

Wang, C., D. Du, and J. D. Richardson (2005), Characteristics of the interplanetary coronal mass ejections in the heliosphere between 0.3 and 5.4 AU, *J. Geophys. Res.*, *110*, A10107, doi:10.1029/2005JA011198.

Wang, Y., C. Shen, S. Wang, and P. Ye (2004), Deflection of coronal mass ejection in the interplanetary medium, *Sol. Phys.*, *222*, 329–343, doi:10.1023/B:SOLA.0000043576.21942.aa.

Wood, B. E., C.-C. Wu, R. A. Howard, D. G. Socker, and A. P. Rouillard (2011), Empirical reconstruction and numerical modeling of the first geoeffective coronal mass ejection of solar cycle 24, *Astrophys. J.*, *729*, 70, doi:10.1088/0004-637X/729/1/70.

Wu, S. T., W. P. Guo, D. J. Michels, and L. F. Burlaga (1999), MHD description of the dynamical relationships between a flux rope, streamer, coronal mass ejection, and magnetic cloud: An analysis of the January 1997 Sun-Earth connection event, *J. Geophys. Res.*, *104*, 14,789–14,802, doi:10.1029/1999JA900099.

Wu, C.-C., C. D. Fry, M. Dryer, S. T. Wu, B. Thompson, K. Liou, and X. S. Feng (2007), Three-dimensional global simulation of multiple ICMEs' interaction and propagation from the Sun to the heliosphere following the 25–28 October 2003 solar events, *Adv. Space Res.*, *40*, 1827–1834, doi:10.1016/j.asr.2007.06.025.

Xie, H., D. Odstrcil, L. Mays, O. C. St. Cyr, N. Gopalswamy, and H. Cremades (2012), Understanding shock dynamics in the inner heliosphere with modeling and type II radio data: The 2010-04-03 event, *J. Geophys. Res.*, *117*, A04105, doi:10.1029/2011JA017304.

Zhang, J., J. Wang, Y. Deng, and D. Wu (2001), Magnetic flux cancellation associated with the major solar event on 2000 July 14, *Astrophys. J.*, *548*, L99–L102, doi:10.1086/318934.

Zhou, Y. F., X. S. Feng, S. T. Wu, D. Du, F. Shen, and C. Q. Xiang (2012), Using a 3-D spherical plasmoid to interpret the Sun-to-Earth propagation of the 4 November 1997 coronal mass ejection event, *J. Geophys. Res.*, *117*, A01102, doi:10.1029/2010JA016380.